processes

MDPI

Article

Influence of Material Composition and Quenching Severity on Numerical Prediction of Residual Stresses and Hardness in Induction-Hardened Cylinders

Aritz Goñi [1,*], Unai Segurajauregi [1], Maialen Areitioaurtena [1], Jon Ander Esnaola [2] and Mario Javier Cabello [1]

[1] Ikerlan Technology Research Centre, Basque Research and Technology Alliance (BRTA), Paseo J.M. Arizmendiarrieta 2, 20500 Arrasate-Mondragon, Spain; usegurajauregi@ikerlan.es (U.S.); mareitioaurtena@ikerlan.es (M.A.); mjcabello@ikerlan.es (M.J.C.)
[2] Department of Mechanics and Industrial Manufacturing, Mondragon Unibertsitatea, Loramendi 4, 20500 Arrasate-Mondragon, Spain; jaesnaola@mondragon.edu
* Correspondence: agoni@ikerlan.es

Abstract: Induction hardening is a heat treatment process that enhances the mechanical properties of materials, improving their resistance to fatigue, fracture, and wear. Unlike conventional methods, induction hardening selectively heats the surface of the material, forming a high-hardness layer while leaving the core relatively unaffected. In addition, it generates a compressive residual stress layer in the surface, which is beneficial for the component service behaviour. This compressive layer progressively decreases, turning tensile at the boundary of the hardened layer, and gradually decreases in the untreated core. This study first focused on the numerical simulation model to analyze the physical mechanisms involved in the process and select the ideal calculation method. Subsequently, the effects of the material's carbon content and the quenching severity on hardness and residual stress formation after the induction hardening of a cylindrical 42CrMo4 steel specimen are examined. For this purpose, a coupled thermo-metallurgical-mechanical finite element model in ANSYS® is employed. The findings underscore the importance of accounting for all factors contributing to stress generation to accurately predict the material's behaviour. Additionally, the results highlight the significant impact of carbon content on the hardness of the hardened layer, as well as the substantial role of quenching medium severity in shaping the axial residual stress profile within the material.

Keywords: induction hardening; numerical model; residual stress; hardness; carbon content; quenching media

Citation: Goñi, A.; Segurajauregi, U.; Areitioaurtena, M.; Esnaola, J.A.; Cabello, M.J. Influence of Material Composition and Quenching Severity on Numerical Prediction of Residual Stresses and Hardness in Induction-Hardened Cylinders. *Processes* **2024**, *12*, 2783. https://doi.org/10.3390/pr12122783

Academic Editor: Masoud Soroush

Received: 19 November 2024
Revised: 30 November 2024
Accepted: 4 December 2024
Published: 6 December 2024

1. Introduction

Induction hardening is an advanced heat treatment technique aimed at producing a hardened surface layer on critical components exposed to high loads and severe contact pressures. This process is generally used to enhance wear resistance, fatigue strength, and durability in steel components, making it a preferred method for applications in automotive, aerospace, and heavy machinery industries, where high-performance materials are essential. This process involves raising the temperature of the workpiece above its austenitization point using induced currents generated by a nearby inductor, through which an alternating current is applied [1]. Following the heating stage, rapid quenching is performed to induce a phase transformation in the microstructure, resulting in the formation of a martensitic layer that provides the necessary hardness to the component. The depth of the hardened layer can extend up to 10 mm, depending on key process parameters such as current, frequency, and process time. In some components, the entire cross-section of the material may undergo hardening.

The primary objective of induction hardening is to create a surface layer with enhanced mechanical strength. Additionally, several studies suggest that induction hardening can lead to changes in the Young's modulus in the treated region. Stasac et al. [2] demonstrate an increase in the Young's modulus for low-alloy steel after induction hardening, while Marthini et al. [3] report a reduction in the Young's modulus for high-carbon steel when the process temperature is increased. This effect, although less prominent than changes in hardness or residual stresses, could influence the stiffness of the hardened layer, potentially enhancing its mechanical performance under certain loading conditions. However, additional effects inherent to the process must be considered, as they can significantly impact the component's service life. One of the most critical effects, due to its influence on fatigue performance, is the development of residual stresses in the treated region. These stresses originate from volumetric changes induced by microstructural transformations or the plastic deformation of the material. Typically, residual stresses exhibit a compressive nature within the first few millimetres of the hardened layer, transitioning to tensile stresses at the boundary of the hardened region, and gradually decreasing in the unhardened zone. The presence of compressive stresses is beneficial for fatigue resistance, as it delays crack initiation and slows crack propagation [4]. Therefore, accurately predicting the residual stresses generated during the induction hardening process is crucial for conducting precise fatigue assessments.

Numerous researchers have focused on developing models to simulate the induction hardening process and predict the residual stress distribution and hardness profiles. Li et al. (2014) [5] performed an analysis aimed at predicting hardness in cylindrical specimens, achieving a strong correlation with experimental data. Hömberg et al. (2016) [6] further refined this approach by incorporating microstructural phase transformations into a coupled model, which showed excellent agreement between numerical results and experimental data. Coupard et al. (2018) [7] developed a comprehensive model to simulate the electromagnetic, thermal, metallurgical, and mechanical fields, using commercial software packages Flux2D®, Metal7®, and MSC Marc® in a sequential approach. The study emphasizes the complexity of predicting the induction hardening process due to the multiphysical interactions involved, presenting considerable computational challenges, particularly when applied to real industrial geometries and processes. Kaiser et al. (2020) [8] investigated the mechanical properties and hardness of AISI 4141 steel after short-time induction quenching, revealing the minimum hardness in the transition zone.

Recent studies have investigated the influence of transformation-induced plasticity (TRIP) on the stress state of induction hardening specimens. Brunbauer et al. (2019) [9] conducted both numerical and experimental analyses to evaluate the evolution of stresses throughout the induction hardening process, as well as the residual stresses' distribution. Findings indicated that TRIP strain significantly affects the stress state by reducing stresses to near-zero values, particularly in the unhardened regions. Taleb et al. (2023) [10] investigated TRIP during the martensitic transformation of 36NiCrMo steel under various complex loading conditions, identifying dissymmetry between tension and compression and introducing the concept of TRIP backstress. A new TRIP model, incorporating backstress effects and stress invariants, successfully aligns with experimental results, addressing the limitations of previous models. Shi et al. (2024) [11] modelled the temperature, microstructure, and residual stress evolution in a 34CrNi3MoA steel marine diesel engine crankshaft during medium-frequency induction hardening, incorporating TRIP mechanism. The simulations, validated by experiments, show that extending heating time improves surface temperature uniformity and increases hardened layer thickness. However, as seen, accurately calculating the TRIP strain involves additional calculation that, although not excessively complex, increases the computational cost in the numerical simulation of the residual stress prediction of an intrinsically complex process. Consequently, developing computationally efficient and accurate simulations of the residual stress profiles generated during induction hardening remains a major challenge in current research, where TRIP mechanism plays a key role in the final residual stress state.

In the induction hardening process, several factors influence the resulting stress state of the hardened sample, with the most significant being the thermal dynamics and the properties of the initial material. Additionally, thermal dynamics can be affected by various aspects, including the specific parameters of the induction process, environmental conditions, and the characteristics of the cooling system, such as the quenching showers, among other factors [1]. These variables collectively play a critical role in shaping the final stress profile of the treated component.

In this study, a previously developed coupled electromagnetic-thermal-mechanical-metallurgical finite element model is employed to predict hardness distribution and residual stresses in cylindrical samples subjected to the induction hardening process. The analysis has two stages: first, the reference model is analysed to try to minimise computational costs without compromising accuracy; secondly, the model is used to investigate the effects of two key aspects: the material's carbon content and the severity of the quenching medium. The findings reveal that carbon content significantly influences the hardness of the hardened layer, while the quenching medium's severity has a marked impact on the residual stress profile, particularly at greater depths within the specimen.

2. Materials and Methods

The case study selected for this research is based on experimental work conducted by the authors in a previous study [12], involving cylindrical samples of 42CrMo4 steel subjected to induction hardening. The specimens had a diameter of 20 mm and a length of 150 mm. Prior to induction hardening, the base material underwent a preliminary quenching and tempering treatment in a furnace, yielding an initial hardness of 320 HV. The chemical composition of the 42CrMo4 steel, determined through optical emission spectrometry, is presented in Table 1, with values expressed as mass percentages.

Table 1. Chemical composition of 42CrMo4 steel measured by optical emission spectrometry [12].

%C	%Mn	%Cr	%Mo	%Si	%P	%S	%Cu
0.450	0.900	1.200	0.300	0.400	0.025	0.035	$\leq$0.400

Induction hardening tests were carried out using a six-coil copper inductor. The average current applied during the tests was 450 A (RMS), with a frequency of 31 kHz for a duration of 11 s, resulting in the generation of a hardened layer of around 2.5 mm thick. After the induction heating stage, the specimens were quenched by immersion in water, which promotes the rapid cooling necessary to induce a martensitic microstructure in the austenitized region. Figure 1 presents both an image and a schematic diagram of the case study. In previous work [12], the residual stresses were measured within the first millimetre of depth using the hole drilling technique with type B strain gauge rosettes, following the non-uniform stress procedure specified in ASTM E837-13a.

To accurately simulate the hardness and residual stress distribution following the induction hardening process, it is critical to determine several material properties, particularly those related to electromagnetic, thermal, microstructural, and mechanical behaviours. Specifically, the magnetic permeability and electrical resistivity as functions of temperature must be characterized. The acquisition and characterization of these properties are detailed in a prior study conducted by the authors [13].

Thermal conductivity and specific heat are essential properties for accurately resolving the thermal behaviour during the induction hardening process. These temperature-dependent properties, particularly at the specimen's surface temperature, were obtained from the study by Montalvo-Urquizo et al. (2013) [14].

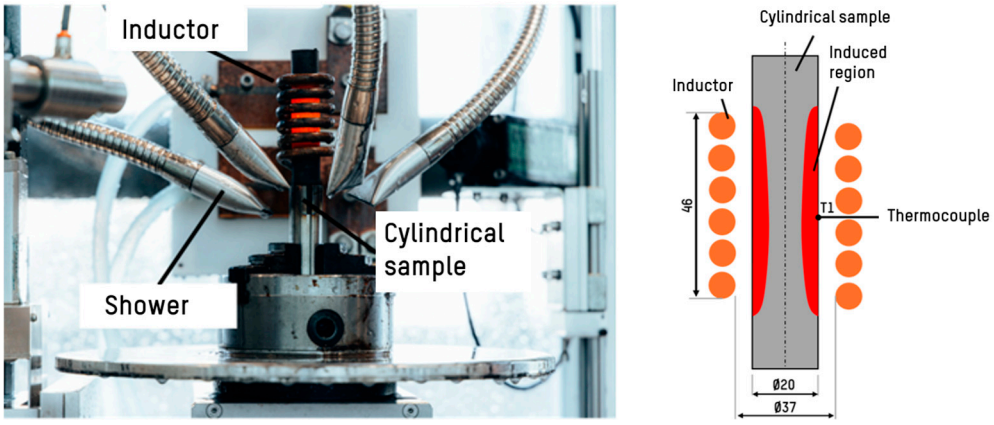

Figure 1. Image and diagram of experimental test.

To obtain the Continuous Cooling Transformation (CCT) diagram for the material used in this study, dilatometry tests were performed. Dilatometry provides critical data on transformation kinetics, including key transformation temperatures (AC_1, AC_3, and M_s), transformation-induced volume changes, and thermal expansion coefficients for various microstructural phases. In this work, the equivalent Coefficient of Thermal Expansion (CTE) method was utilized, where the CTE is calculated based on relative changes in length obtained by dilatometric measurements. As shown in Figure 2, two distinct CTE values were obtained, corresponding to the different microstructural phases and their transformations. This equivalent CTE approach accounts not only for the specific thermal expansion of each phase but also for the volumetric expansion or contraction associated with phase transformations.

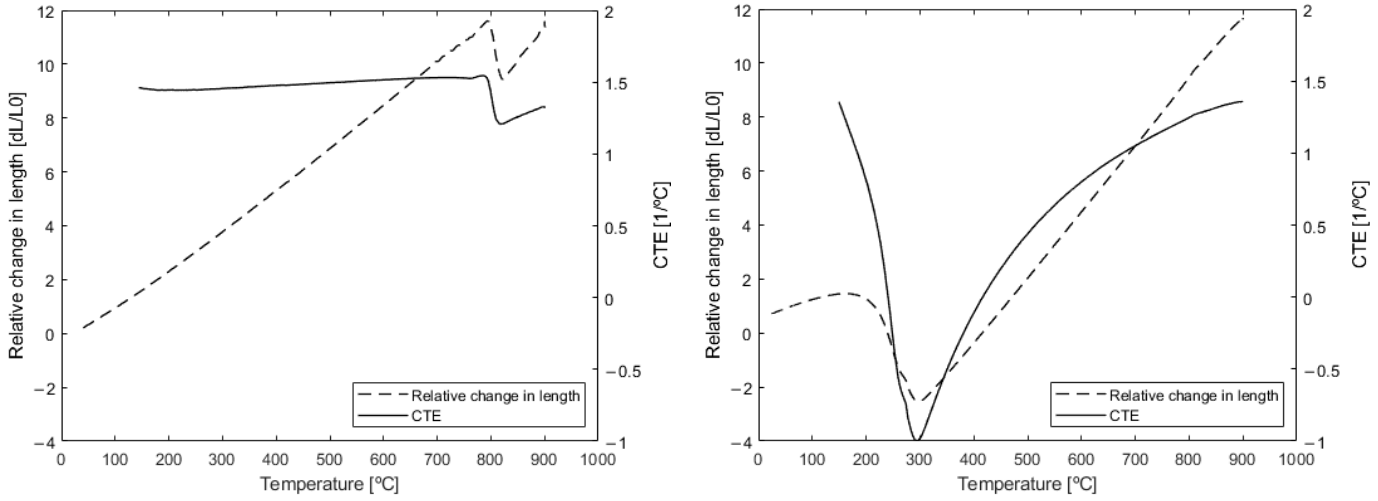

Figure 2. Relative change in length resulting from dilatometry test [12] and Equivalent Coefficient of Thermal Expansion. Values presented for (**a**) transformation to austenite and (**b**) transformation to martensite.

To determine the mechanical properties of the material, the relationship between yield strength (σ_{Y_0}) and hardness, as defined in Equation (1) [15], was applied, where HV represents the Vickers hardness. Additionally, both yield strength and Young's modulus were assumed to decrease with increasing temperature, in accordance with previous findings by the authors [12]. Poisson's ratio was kept constant at 0.3 throughout the analysis.

These mechanical properties were incorporated into the numerical model to improve its predictive accuracy.

$$\sigma_{Y_0} = -90.7 + 2.88HV \quad (1)$$

3. Numerical Model of Induction Hardening

The induction hardening process involves the interaction of multiple physical phenomena, including electromagnetic, thermal, microstructural, and mechanical aspects. Accurately capturing these complex interactions is essential for any numerical simulation model. This study utilizes a coupled numerical model, previously developed by the authors [12], that fully integrates these interactions. The details of the model are outlined below.

The model comprises three distinct stages. First, an electromagnetic analysis is performed at room temperature using ANSYS Maxwell Release 2019R1, where the magnetic field strength (H) is calculated for each node. In the second stage, conducted in ANSYS Mechanical Release 2020R1, a semi-analytical approach is applied using Ansys Parametric Design Language (APDL). This stage imports the magnetic field strength obtained at room temperature, adjusts the electromagnetic properties according to the surface temperature of the specimen, and analytically computes the heat generated by the electromagnetic field. The finite element method is then used to calculate the resulting temperature distribution along the workpiece based on the generated heat. In the final stage, User Programmable Features (UPFs) subroutines, written in Fortran, are employed to implement the constitutive material model developed by the authors. The incorporation of the thermal distribution at this stage is crucial, as many material properties, including mechanical and microstructural characteristics, are temperature dependent.

The electromagnetic field in the induction hardening process is governed by Maxwell's equations, which describe the electromagnetic phenomena occurring during induction heating. These equations allow for the calculation of the heat generated within the specimen [16]. Once heat generation is determined, the heat conduction equation is solved to model the resulting temperature distribution throughout the material. Finite element analysis of the electromagnetic field is computationally demanding, particularly for complex industrial geometries. To mitigate this challenge, the authors developed and validated the previously described semi-analytical approach in which Maxwell's equations are solved only once at room temperature and electromagnetic properties are calculated analytically based on the specimen's temperature. This approach significantly reduces computational costs while maintaining accuracy. For more comprehensive details on the semi-analytical approach, readers can refer to the work of Areitioaurtena et al. (2021) [13]. During the cooling phase, a convective heat transfer coefficient, derived from experimental temperature measurements, was applied. This coefficient was determined using the method described by Liščić and Filetin [17] and is shown in Figure 2b.

The fraction of transformed austenite (f_y) was modelled using the modified Koistinen and Marburger Equation (2) [18]. Additionally, the non-diffusive martensitic transformation ($f_{\alpha'}$) was calculated using the relationship established by Koistinen and Marburger [19], expressed in Equation (3).

$$f_y = exp\left(k\frac{AC_1 - T}{AC_1 - AC_3}\right) \quad (2)$$

$$f_{\alpha'} = f_y[1 - \exp(-\alpha_M(M_s - T))] \quad (3)$$

where AC_1, AC_3, and M_s represent the austenite transformation start temperature, austenite transformation end temperature, and martensite start temperatures, respectively. The coefficients k and α_M are typically assumed to be constant, with a value of 0.011/K.

The hardness of the material is dependent on its microstructural phases and chemical composition. The Vickers hardness of each phase can be estimated using the equations

proposed by Maynier et al. (1977) [20], which provide phase specific hardness values based on these parameters.

$$HV_M = 127 + 949C + 27Si + 11Mn + 8Ni + 16Cr + 21\log(V_r) \quad (4)$$

where V_r represents the cooling rate at 700 °C expressed in °C/h and the chemical elements are given in mass percentages as outlined in Table 1. A linear mixing rule is applied to determine the overall hardness of the specimen, which is derived from the contributions of each microstructural phase.

The calculation of the residual stresses during the induction hardening process relies on the total strain rate tensor represented by Equation (5). To implement this equation within the reference model, it was necessary to modify and use the USERMAT and USERTHSTRAIN subroutines of the ANSYS Mechanical Release 2020R1. These subroutines allowed for the dynamic modification of material properties throughout the induction hardening process, accounting for the temperature-dependent behaviour and phase transformations.

$$\dot{\varepsilon}_{ij} = \dot{\varepsilon}_{ij}^{el} + \dot{\varepsilon}_{ij}^{pl} + \dot{\varepsilon}_{ij}^{th} + \dot{\varepsilon}_{ij}^{tr} + \dot{\varepsilon}_{ij}^{tp} \quad (5)$$

where $\dot{\varepsilon}_{ij}^{el}$, $\dot{\varepsilon}_{ij}^{pl}$, $\dot{\varepsilon}_{ij}^{th}$, $\dot{\varepsilon}_{ij}^{tr}$, $\dot{\varepsilon}_{ij}^{tp}$ represent the contribution from elastic deformation, plastic deformation, thermal deformation, transformation deformation, and transformation-induced plasticity (TRIP), respectively.

Elastic deformation: The constitutive stress–strain relationship for elastic deformation is governed by Hooke's law, as described in Equation (6). This relationship is based on the material's Young's modulus (E) and Poisson's ratio (ν). Hooke's law provides a linear relationship between stress and strain within the elastic limit of the material, enabling accurate predictions of material behaviour under elastic loading conditions.

$$\sigma = E\varepsilon_e \quad (6)$$

Plastic deformation: In this study, a bilinear isotropic strain hardening model is employed to characterize plastic deformation, simplifying the strain hardening behaviour as shown in Equation (7). Additionally, yield stress is updated at each time increment to reflect changes in material properties due to plastic deformation, as described in Equation (8).

$$\sigma = K\varepsilon_p \quad (7)$$

$$\sigma_Y = \sigma_{Y_0} + K\varepsilon_p \quad (8)$$

where σ_{Y_0} represents the initial temperature-dependent yield strength for each microstructural phase and K denotes the tangent modulus of the material. In this study, the tangent modulus is defined as 10% of Young's modulus.

Thermal deformation: Thermal deformations arise from isotropic expansion and contraction of the material in response to temperature variations. Each microstructural phase exhibits a distinct Coefficient of Thermal Expansion (CTE), which was determined through dilatometry tests.

Transformation deformation: Phase transformations induce volumetric changes due to the rearrangement of atomic structures. The equivalent CTE approach used in this study, as presented in Figure 2b, allows for the simultaneous consideration of both thermal and transformation deformations thereby capturing the effects of phase changes on overall material behaviour.

Transformation-induced plasticity (TRIP): TRIP strain refers to the plastic deformation that occurs during microstructural transformations under non-zero stress conditions [21]. The generalized expression for multi-axial stress states is formulated as shown in Equation (9), with a specific description provided in Equation (10) as outlined

by Kaiser et al. (2020) [8]. In this study, TRIP strain is calculated exclusively during the cooling phase.

$$\dot{\varepsilon}_{ij}^{tp} = \frac{3}{2} K \sigma'_{ij} g(f) \frac{df}{dt} \tag{9}$$

$$g(f) = f(2 - f) \tag{10}$$

where σ'_{ij} denotes the deviatoric stress tensor, f represents the fraction of the existing microstructural phase, and K represents the Greenwood-Johnson parameter. For 42CrMo4 steel, a K value of 42×10^{-6} MPa^{-1} is used [20].

As previously mentioned, the multiphysics simulation model was implemented in ANSYS® Release 2020R1, using a combination of the APDL programming language and User Programmable Features (UPF) subroutines developed in Fortran. The model utilizes an axisymmetric finite element model configuration consisting of 10k nodes. Given the significant deformations that occur during phase transformations, small time increments are required at certain stages of the process to ensure convergence. The numerical model presented here was validated in a prior study by the authors. For a detailed account of the validation process, readers can refer to Areitioaurtena et al. (2022) [12]. This validated numerical simulation model of induction hardening is applied in the current work.

The total computation time for the entire process—including the electromagnetic solution, semi-analytical modelling of the induction heating, and subsequent mechanical analysis—was around 2 h. However, when applied to more complex three-dimensional geometries and extended processes, the computation time required to obtain stress results increased significantly, often extending to a full day or more, with some cases experiencing convergence issues. Consequently, a sensitivity analysis was conducted by simplifying the mechanical analysis to evaluate the impact of various contributions to stress generation. The objective of this analysis was to assess the feasibility of omitting certain elements from the numerical model to reduce computation time without compromising accuracy. For this purpose, three different calculation models were developed. These models are graphically illustrated in Figure 3 and described below.

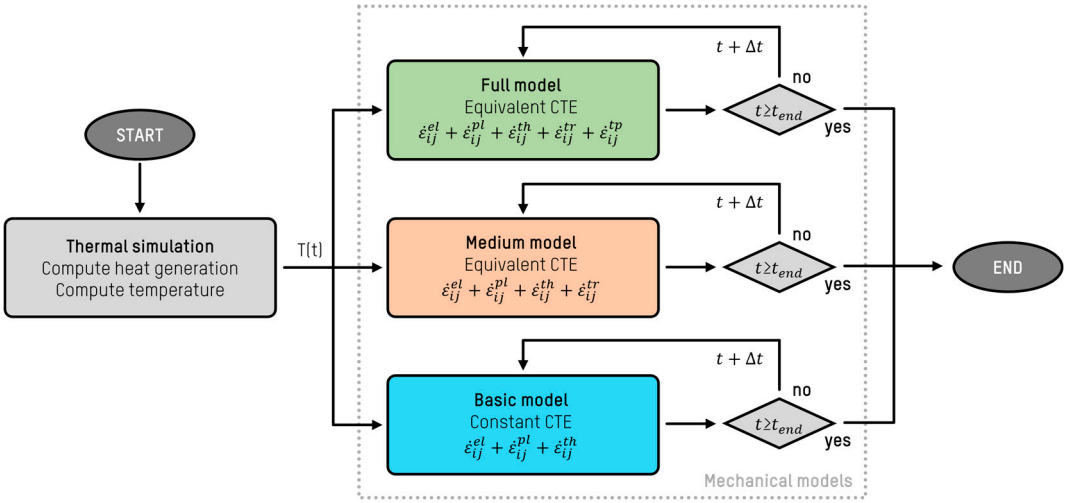

Figure 3. Analysed alternative numerical simulation models.

Full model: This comprehensive model incorporates all previously discussed aspects, including all five components of Equation (5) (elastic, plastic, thermal, transformation, and TRIP strains), the equivalent CTE approach, and the effects of hardness and microstructural phases on the mechanical properties.

Medium model: This reduced model retains most features of the Full model but excludes the TRIP component from Equation (5).

Basic model: The simplest model further decreases the complexity of the Medium model by also removing the transformation strain from Equation (5). The temperature-dependent equivalent CTE is replaced with a constant CTE, leaving only three strain rate components in the simulation: elastic, plastic, and thermal deformations.

4. Results and Discussion

Figure 4a illustrates the layout of the 2D axisymmetric model employed in this analysis. The region designated for comparison between experimental and numerical results—specifically concerning hardness and residual stresses—is highlighted with a red arrow. Meanwhile, Figure 4b shows the fine meshing required for the mechanical solution, which is crucial for ensuring a detailed and accurate representation of the stress and hardness distributions throughout the specimen.

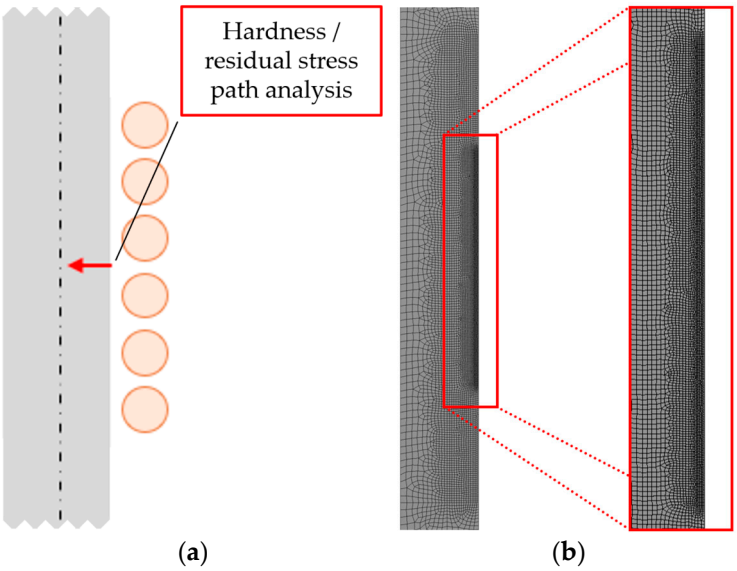

Figure 4. (**a**) Two-dimensional axisymmetric model used for analysis, highlighting path for hardness and residual stress evaluation, and (**b**) mesh of mechanical problem.

The model discretization was designed based on thermal gradients. In the region near the surface, specifically around the area impacted by the inductor, a fine mesh size of 0.1 mm was applied. In contrast, regions farther away were discretized with a coarser mesh size of 1 mm. The intermediate zones featured a transition in element size. The mesh consisted of second-order hexahedral elements with full integration, resulting in a total of 27,750 nodes and 9043 elements.

4.1. Influence of Volume Expansion Mechanism

Figure 5a presents the axial residual stress results following the whole induction hardening process for each calculation model. It is observed that the reference Full model and the Medium model present similar results while the Basic model presents a higher discrepancy. In addition, Figure 5b illustrates the axial residual stress profile along the radial path detailed in Figure 4a, comparing results obtained from the Full, Medium, and Basic calculation models against experimentally measured residual stress values. The model predicts a typical residual stress pattern observed after an induction hardening process where (i) the hardened zone experiences compressive stresses that (ii) shifts to tensile stress at the transition zone, (iii) reaches the maximum tensile peak stress at the end of the transition zone, and (iv) stabilizes at lower tensile stress values.

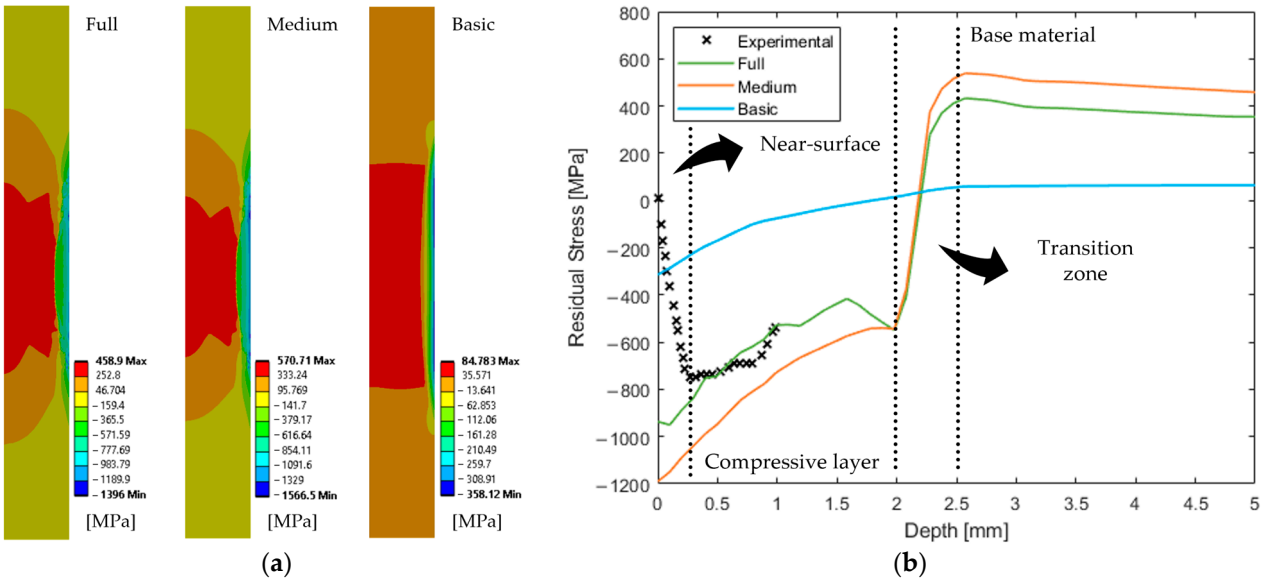

Figure 5. (**a**) Final stress state of three calculation models and (**b**) comparison of axial residual stress in depth according to calculation model and experimental measurements.

The comparison of different calculation models yields significant insights regarding their effectiveness and computational efficiency. The Basic model, while capable of producing results within just 5 min of the simulation time, demonstrates considerable divergence from both experimental measurements. Besides the computational time saving, the lack of accuracy, as depicted in Figure 5, indicates that it does not capture the necessary mechanism to predict residual stress adequately.

In contrast, the Medium and Full models require around 14 and 15 min of computation time, respectively. Figure 5b shows an almost identical slope in the hardened zone for both calculation models. This slope may be attributed to various factors, including potential differences in cooling rates throughout the depth of the hardened layer or the stress equilibrium within the entire hardened sample.

From a quantitative perspective, the numerical results are compared with experimental data. As highlighted by Areitioaurtena et al. [12], the discrepancies observed in the near-surface region may be related to some factors such as surface roughness, incorrect alignment of the reference zero at the surface, or the small curvature of Ø20 mm specimens. For that reason, the near-surface region is neglected for the comparison between experimental and numerical results. It is observed that the Full model matches adequately with experimental RS measurements in the compressive layer, a critical region where fatigue-induced failures typically occur. In that zone, a maximum discrepancy of 120 MPa and a mean error of 6% are observed. In contrast, the Medium model overestimates the compressive residual stress magnitude with an offset of around 200 MPa compared to the Full model and a 30% mean error in the compressive layer. This discrepancy is attributed to the omission of TRIP mechanism effects. Despite the discrepancy, the results from the Medium model remain reasonably aligned with the experimental data. Later, in the transition zone, the numerical results of the Full and Medium models are practically identical since their only difference is the TRIP mechanism, which only affects the hardened zones. Finally, in the base material, the differences are similar to those found in the compressive layer due to the mechanical equilibrium of the workpiece.

Considering the slight time differences between the Medium and Full models, the Full model emerges as the preferable choice for accurate stress analysis, despite its longer computation time.

4.2. Influence of Carbon Content

Carbon content is the most influencing alloying element in the final hardness of martensite, as evidenced in Equation (4). Thus, the carbon content in the induction hardening processes where high martensite transformation occurs, as the reference case of 42CrMo4 steel with martensite transformation over 98% in the hardened zone, could be determinant in the obtained hardness. As material composition, including carbon content, present minor variations among different suppliers, in the present study, the influence of a carbon content range from 0.39% to 0.45% by mass in the obtained hardness level of induction-hardened 42CrMo4 specimens was analysed. Consequently, the influence of different carbon content on both the hardness and the residual stress profile was examined.

For that purpose, the reference case of 0.45% carbon was compared with materials containing 0.39% and 0.42% carbon content cases. Figure 6b illustrates the hardness profile within the first 5 mm of the three cases. It is observed that the hardened zone, which extends to a depth of 2 mm, presents hardness magnitude values that can vary from 650 to 720 HV from the lowest to the highest carbon content case. Figure 6a shows the final hardness result where the hardened zone is highlighted in red. This analysis underscores the critical role of carbon content in determining the hardness profile in induction-hardened steel. The results demonstrate a difference of over 70 HV between the most extreme cases, highlighting how even slight variations in carbon content can significantly affect the hardness achieved through induction hardening. Results indicate that these variations significantly impact the final hardness of the material following the induction hardening process.

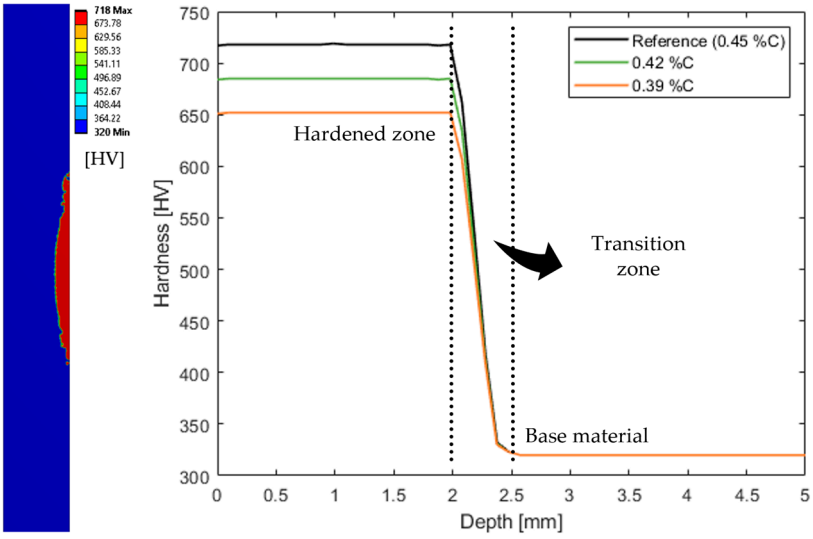

(**a**) (**b**)

Figure 6. (**a**) The FEM result of the hardness distribution for the reference simulation and (**b**) a comparison of the hardness in the first millimetres of depth for the different carbon contents.

Figure 7, depicting the axial residual stress profiles, reveals that while carbon content has a notable impact on hardness, it has a relatively slight effect on residual stresses. The maximum variation in axial residual stress due to carbon is under 100MPa. This slight difference occurs because higher hardness (caused by increased carbon content) raises the yield strength of the material according to Equation (1). Consequently, for the same strain level, the material undergoes less plastic deformation, leading to lower residual stress generation. This analysis suggested that while carbon content is crucial for achieving the desired hardness in induction-hardened components, its influence on residual stress is comparatively less significant.

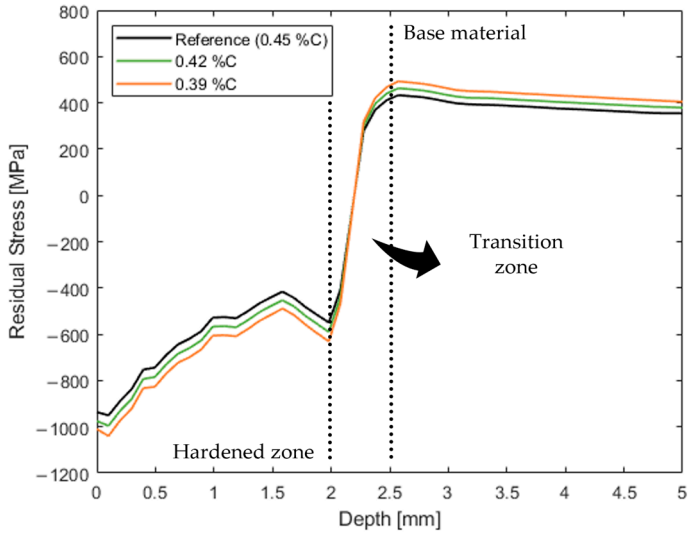

Figure 7. Comparison of axial residual stress in first millimetres of depth for different carbon contents.

4.3. Influence of Quenching Severity

The simulation model's investigation into the impact of cooling severity on hardness and axial residual stresses after the induction hardening process provides important insights into how different quenching media affect the material properties. Figure 8a shows the different cooling scenarios analysed, where the baseline cooling condition is represented by the black curve. Two additional cases, represented by the green and orange curves, show the effects of reducing the convection coefficient by factors of 0.66 and 0.33, emulating less severe quenching media. Figure 8b highlights the time evolution of temperature at two key locations: the surface centre of the hardened zone and at a depth of 2 mm beneath the surface. These results illustrate that cooling severity significantly impacts the cooling rate. For instance, under the baseline quenching condition, the material cools down to 100 °C in around 3 s, while the less severe cooling case (extra-light convection) takes about 10 s to reach the same temperature. This prolonged cooling time can influence the transformation dynamics, particularly in achieving the desired martensitic microstructure.

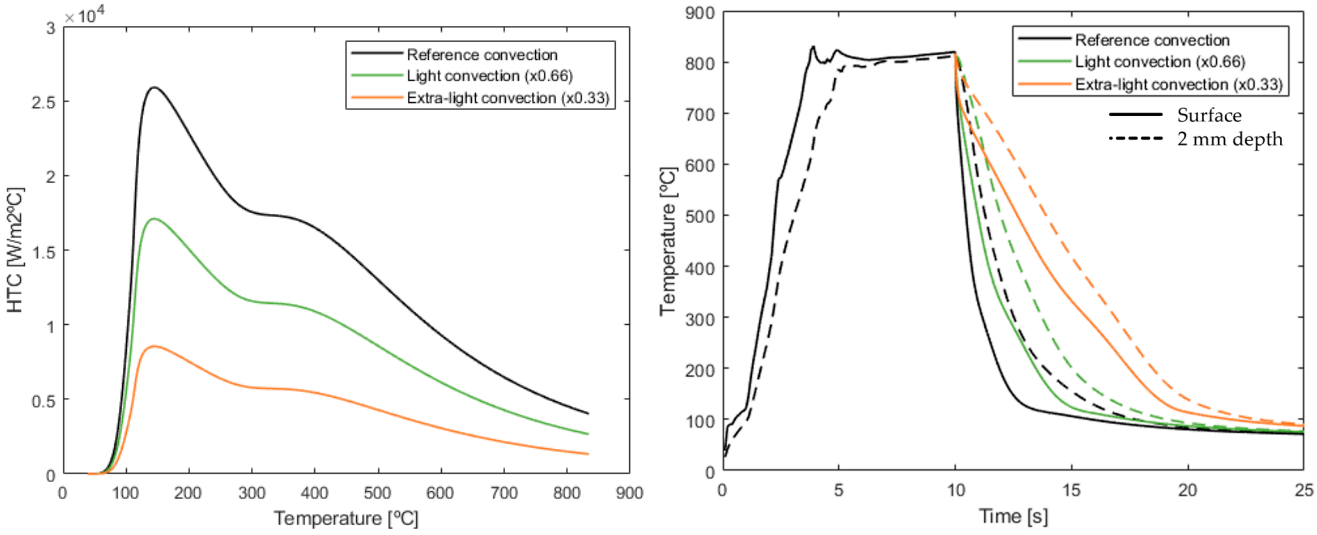

(**a**) (**b**)

Figure 8. (**a**) Convection heat transfer coefficient as function of surface temperature of workpiece and (**b**) evolution of temperature in surface central point and 2 mm depth.

The simulation results demonstrate that variations in quenching severities have a noticeable effect. However, when considering hardness, the impact of quenching severity, represented by the convection coefficient, is very slight. Figure 9 shows the hardness profile in the first few millimetres of depth along the path marked in Figure 4a.

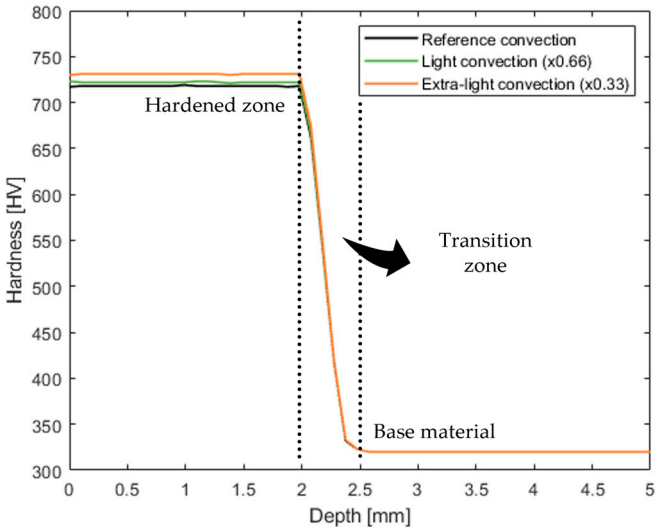

Figure 9. Hardness profile in first millimetres of depth as function of cooling severity.

A crucial factor to consider is the cooling rate at 700 °C, which influences the final hardness achieved through the cooling transformation, as outlined by Equation (4). The cooling rate at this temperature directly affects the martensite formation thereby impacting both hardness and residual stresses generated within the hardened layer. As the cooling severity decreases (due to less aggressive quenching), the resultant reduction in cooling rate may lead to softer microstructures, potentially decreasing hardness and adversely affecting the mechanical performance of the material.

Figure 9 illustrates the clear distinction among the hardened zone, the transition zone, and the base material, where the variations resulting from different quenching severities are limited to just 15 HV. It is also observed that in the hardened zone, the hardness value is almost constant on the surface and at the end of the hardened layer (2 mm). These observations are summarized in Table 2, which presents the cooling rate values at 700 °C at both the surface and at a depth of 2 mm, along with their influence on the hardness model as described in the latter part of Equation (4). Consequently, the minor differences in the hardness model observed in this study among the various cooling methods and analysis location are thus justified.

Table 2. Cooling rate and hardness with varying convection severity for surface and 2 mm depth.

		Reference Convection	Light Convection	Extra-Light Convection
Surface	Cooling rate [°C/s]	−673	−328	−101
	Hardness [HV]	**724**	**718**	**707**
2 mm	Cooling rate [°C/s]	−288	−171	−68
	Hardness [HV]	**716**	**712**	**703**

The results for axial residual stress within the first millimetres of depth, as illustrated in Figure 10, provided valuable insights into the cooling dynamics associated with different quenching methods. The light convection cooling scenario exhibits thermal cooling characteristics that closely resemble those of the baseline quenching condition, resulting in nearly identical stress results. In contrast, the extra-light convection cooling method produces a compression pattern around 300 MPa lower than that observed in the refer-

ence cooling condition. This method also reveals a similar transition to the other cases, alongside a tensile pattern around 200 MPa lower than the values recorded for the other cooling conditions. The significant deviation in cooling thermal dynamics associated with the extra-light convection method accounts for the observed differences in residual stress compared to the reference and light convection cooling conditions.

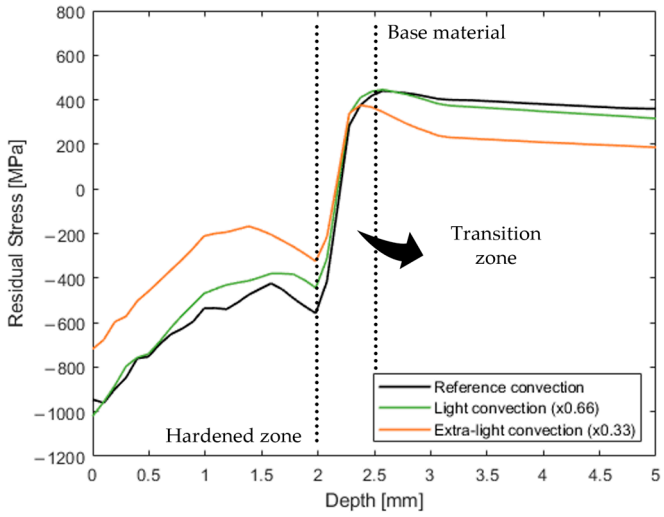

Figure 10. The axial residual stress profile in the first millimetres of depth as a function of the cooling severity.

Another critical consideration is the internal zone of the specimen. This region, located just beneath the hardened layer, is where cracks initiate and propagate, particularly in scenarios such as Rolling Contact Fatigue. Therefore, the magnitude and position of the maximum tensile stress peak are critical factors to consider. Thus, accurately predicting the tensile residual stress is essential for understanding the generation of the cracks. Figure 10 illustrates that the severity of the quenching medium affects the axial residual stress within the tensile region: higher thermal gradients result in increased stresses (both compressive and tensile). This variation emphasizes the necessity of precise control over the quenching conditions.

5. Conclusions

A finite element model, previously developed and validated by the authors, was employed to simulate the effects of induction hardening and to analyse the contribution of the different volume expansion mechanism, as well as the influence of the material carbon content and quenching media severity on hardness and residual stresses after the process. The following conclusions were drawn:

- Despite the increased computational cost, it is essential to consider all contributors to residual stresses generation as outlined in Equation (5). This comprehensive approach provides a more accurate prediction of the residual stress profile within the workpiece.
- The carbon content significantly affects the hardness of the hardened layer, with variations of up to 70 HV observed when the carbon level increases from approximately 0.39% to 0.45%. However, its influence on the axial residual stress profile is minimal. In the compression zone, stress variations reach only about 80 MPa, and in the tensile zone, the effect is even less pronounced.
- The quenching media has negligible influence on the hardness of the hardened layer due to the limited role of cooling rate variations in the hardness model. However, the slight differences in hardness translate into variations in residual stresses. Specifically, extra-light cooling consistently reduces axial residual stresses compared to the baseline quenching media, with differences of up to 200 MPa.

Author Contributions: Conceptualization, A.G., U.S. and J.A.E.; methodology, A.G.; validation, M.A.; investigation, A.G.; writing—original draft preparation, A.G. and U.S.; writing—review and editing, U.S. and J.A.E.; visualization, M.J.C.; supervision, U.S. and J.A.E.; project administration, M.J.C.; funding acquisition, U.S. and M.J.C. All authors have read and agreed to the published version of the manuscript.

Funding: This research was funded by the Basque Government through the 2023 Industrial Doctorate Training Aid Program, grant number BIKAINTEK 020-B2/2023.

Data Availability Statement: The data supporting the findings of this study are available from the corresponding author upon reasonable request.

Conflicts of Interest: Authors Aritz Goñi, Unai Segurajauregi, Maialen Areitioaurtena and Mario Javier Cabello were employed by the company Ikerlan Technology Research Centre. The remaining authors declare that the research was conducted in the absence of any commercial or financial relationships that could be construed as a potential conflict of interest.

References

1. Rudnev, V.; Loveless, D.; Cook, R.L. *Handbook of Induction Heating*, 2nd ed.; CRC Press—Taylor & Francis Group: Boca Raton, FL, USA, 2017.
2. Stasac, C.O.; Tomse, A.D.; Arion, M.N.; Bandici, L.; Hathazi, F.I. Effect of heat-treatment process on magnetic characteristics of grain-oriented electrical steel. *Processes* **2024**, *12*, 2045. [CrossRef]
3. Marthini, V.; Alhelali, I.A.A.; Afendi, M.; Majid, M.; Syafiq, W.M. Effect of Quenching on the Mechanical Properties of Carbon Steel for Hammer Mill. *J. Phys. Conf. Ser.* **2021**, *2051*, 012057. [CrossRef]
4. Schijve, J. *Fatigue of Structures and Materials*, 2nd ed.; Springer: Amsterdam, The Netherlands, 2009.
5. Li, Z.; Gerguson, B.L.; Nemkov, V.; Goldstein, R.; Jackowski, J.; Fett, G. Stress Generation in an axle shaft during induction hardening. *J. Mater. Eng. Perform.* **2014**, *23*, 4170–4180. [CrossRef]
6. Hömberg, D.; Liu, Q.; Montalvo-Urquizo, J.; Nadolski, D.; Petzold, T.; Schmidt, A.; Schulz, A. Simulation of multi-frequency-induction-hardening including phase transitions and mechanical effects. *Finite Elem. Anal. Des.* **2016**, *121*, 86–100. [CrossRef]
7. Coupard, D.; Palin-luc, T.; Bristiel, P.; Ji, V.; Dumas, C. Residual stresses in surface induction hardening of steels: Comparison between experiment and simulation. *Mater. Sci. Eng. A* **2008**, *487*, 328–339. [CrossRef]
8. Kaiser, D.; Damon, J.; Mühl, F.; de Graaf, B.; Kiefer, D.; Dietrich, S.; Schulze, V. Experimental investigation and finite-element modeling of the short-time induction quench-and-temper process of AISI 4140. *J. Mater. Process. Technol.* **2020**, *279*, 116485. [CrossRef]
9. Brunbauer, S.; Winter, G.; Antretter, T.; Staron, P.; Ecker, W. Residual stress and microstructure evolution in steel tubes for different cooling conditions—Simulation and verification. *Mater. Sci. Eng. A* **2019**, *747*, 73–79. [CrossRef]
10. Taleb, L.; Duchaussoy, A.; Jimenez, J. Transformation induced plasticity in ferritic steels: New experiments and updated modeling. *Int. J. Plast.* **2023**, *171*, 103775. [CrossRef]
11. Shi, X.; Lv, C.; Li, G.; Wang, K.; Chen, J.; Tang, J. Study on induction hardening performance of 34CrNi3MoA steel crankshaft. *Front. Mater.* **2023**, *10*, 1240087. [CrossRef]
12. Areitioaurtena, M.; Segurajauregi, U.; Fisk, M.; Cabello, M.; Ukar, E. Numerical and experimental investigation of residual stresses during the induction hardening of 42CrMo4 steel. *Eur. J. Mech.-A/Solids* **2022**, *96*, 104766. [CrossRef]
13. Areitioaurtena, M.; Segurajauregi, U.; Akujarvi, V.; Fisk, M.; Urresti, I.; Ukar, E. A semi-analytical coupled simulation approach for induction heating. *Adv. Model. Simul. Eng. Sci.* **2021**, *8*, 14. [CrossRef]
14. Montalvo-Urquizo, J.; Liu, Q.; Schmidt, A. Simulation of quenching involved in induction hardening including mechanical effects. *Comput. Mater. Sci.* **2013**, *79*, 639–649. [CrossRef]
15. Pavlina, E.J.; Van Tyne, C.J. Correlation of yield strength and tensile strength with hardness for steels. *J. Mater. Eng. Perform.* **2008**, *17*, 888–893. [CrossRef]
16. Fisk, M.; Lindgren, L.E.; Datchary, W.; Desmukh, V. Modelling of induction hardening in low alloy steels. *Finite Elem. Anal. Des.* **2017**, *144*, 61–75. [CrossRef]
17. Liščić, B.; Filetin, T. Measurement of quenching intensity, calculation of heat transfer coefficient and global database of liquid quenchants. *Mater. Inžinierstvo* **2012**, *19*, 52–63.
18. Xia, J.; Jin, H. Numerical modeling of coupling thermal-metallurgical transformation phenomena of structural steel in the welding process. *Adv. Eng. Soft.* **2017**, *115*, 66–74. [CrossRef]
19. Koistinen, D.; Marburger, R. A general equation prescribing the extent of the austenite-martensite transformation in pure iron-carbon alloys and plain carbon steels. *Acta Metal.* **1959**, *7*, 59–60. [CrossRef]

20. Maynier, P.; Jungmann, B.; Dollet, J. Creusot-loire system for the prediction of the mechanical properties of low alloy steel products. *Hardenability Concepts Appl. Steel* **1978**, *1977*, 518–545.
21. Rohde, J.; Jeppson, A. Literature review of heat treatment simulations with respect to phase transformation, residual stresses and distortion. *Scand. J. Metal.* **2000**, *29*, 47–62. [CrossRef]